




# Synthesis of Ag<sub>2</sub>O Coated TiO<sub>2</sub> Nanoparticles by Sonochemically Activated Methods for Enhanced Photocatalytic Activities

Anjali Athawale<sup>1</sup> · Anuja Bokare<sup>1</sup> · Hema Singh<sup>1</sup> · Van-Huy Nguyen<sup>2</sup> · Dai-Viet N. Vo<sup>3</sup> · Deepak Kumar<sup>4</sup> · Ajit Sharma<sup>4</sup> 

Published online: 15 September 2020  
© Springer Science+Business Media, LLC, part of Springer Nature 2020

## Abstract

TiO<sub>2</sub> nanoparticles were successfully synthesized by sol-hydrothermal (SH) method using sonochemically activated precursors. Sonochemical activation yields product bearing desirable crystallinity at relatively lower temperature in comparison with conventional SH method. Glycine was used as a mineralizer in the ultrasound activation process which suppress the formation of brookite phase (of TiO<sub>2</sub>) observed in the sonochemically activated sample. TiO<sub>2</sub> sample synthesized in presence of Glycine [SA-SH(GLY)] was further modified by coating Ag<sub>2</sub>O nanoparticles by sonochemical (SD-Ag) and photochemical (PD-Ag) methods. The deposition by sonochemical method yields product with better crystallinity, high surface area and improved optical properties. Morphological investigations confirm the formation of rounded cube and cube shaped Ag<sub>2</sub>O particles in the sonochemical and photochemical methods respectively. Photoactivities of the catalysts were investigated in terms of degradation of methyl orange (MO) dye contaminated aquatic waste. Equilibrium of MO photo-degradation was achieved within about 90 min with removal efficiencies of 99.9, 67.1, and 44.4% for SD-Ag, PD-Ag, and SA-SH-(GLY) samples, respectively at 50 mg/L of MO dye concentration. The high photo-catalytic activity of SD-Ag sample was observed for MO photo-degradation, which is attributed to the improved properties like crystallinity, visible light absorption capacity and higher surface area.

---

✉ Anjali Athawale  
agbed@chem.unipune.ac.in

✉ Deepak Kumar  
deepak.sharma99967@gmail.com

✉ Ajit Sharma  
ajitsharma2003@gmail.com

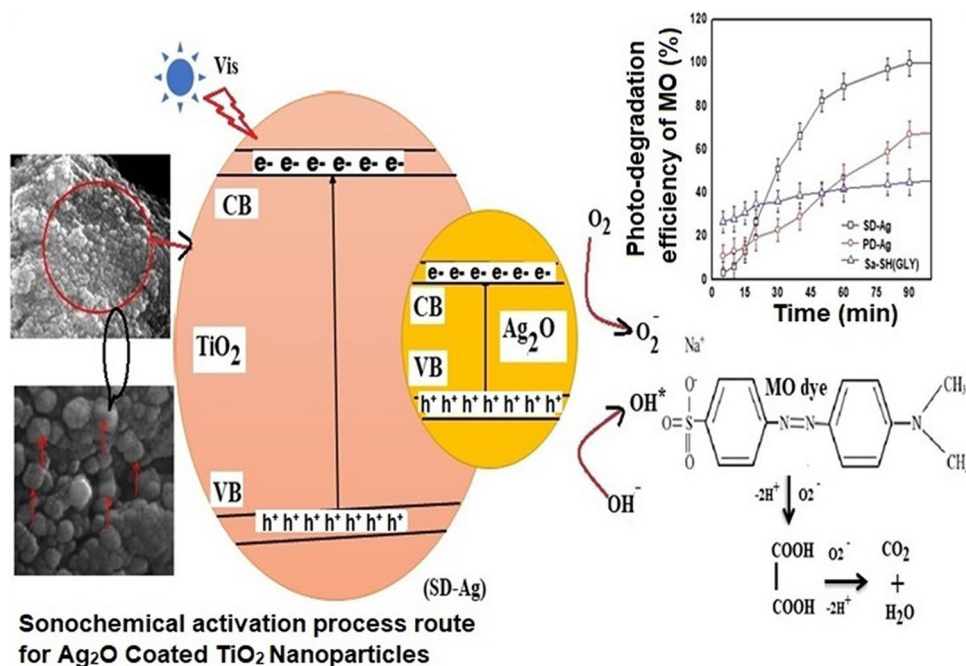
<sup>1</sup> Department of Chemistry, University of Pune, Pune 411007, India

<sup>2</sup> Institute of Research and Development, Duy Tan University, Da Nang 550000, Vietnam

<sup>3</sup> Center of Excellence for Green Energy and Environmental Nanomaterials (CE@GrEEN), Nguyen Tat Thanh University, Ho Chi Minh City 755414, Vietnam

<sup>4</sup> Department of Chemical Sciences, School of Chemical Engineering and Physical Sciences, Lovely Professional University, Phagwara 144411, India

Graphic Abstract



Advance route of sonochemical activation process for synthesis of Ag<sub>2</sub>O co-capped TiO<sub>2</sub> nanocomplex for MO photo-degradation

**Keywords** Sonochemical deposition · Photochemical deposition · Cube shaped ag<sub>2</sub>O nanoparticles · Photocatalysis

1 Introduction

Material synthesis is the integral part of modern material research and industrial development. TiO<sub>2</sub> is one of the most studied compounds in material science (with more than 40,000 publications over the past 10 years) [1–3]. Synthesis of TiO<sub>2</sub> nanomaterials with defined properties such as nanocrystallinity, pure anatase phase, high surface area and lower degree of recombination are the most important prerequisites for its various applications [4–6]. It has already been reported that the properties of the TiO<sub>2</sub> nanomaterials can be tailored by varying the methods of synthesis [7, 8] such as sol–gel method [9], co-precipitation method [10], hydrothermal method [11], polyol method [12], combustion method [13], microwave method [14], sonochemical method [15] etc. Each of these methods has its own advantages and limitations. Sol–gel synthesis yields pure crystalline powders of TiO<sub>2</sub> with excellent control of the composition but requires high calcination temperature to obtain the crystallinity which affects the surface areas adversely [16]. Hydrothermal method is a low temperature process with a controlled particle size distribution and high surface areas but it involves the drawbacks like prolonged reaction times and safety issues related to high pressure processing [17].

Considering the advantages and limitations of the above mentioned methods, it was thought that synthesis of TiO<sub>2</sub> if carried out by combinatorial method would yield a product having the desirable properties i.e. phase, crystallinity as well as high surface area and good catalytic activity. Accordingly, in the present work, hydrothermal synthesis of TiO<sub>2</sub> was carried out by using sonochemically treated precursor solutions. The products so obtained, were found to be highly crystalline (at relatively lower temperature) in nature with anatase as the major phase together with small fraction of brookite. Brookite phase could be completely eliminated by adding Glycine as a mineralizer during sonochemical activation of the precursors.

Taking into account the advantages of sonochemical synthesis, this method was further used for noble metal (silver, Ag) deposition on the surface of TiO<sub>2</sub> nanoparticles. Deposition was also carried out by conventional photochemical method and comparison has been made between these two methods on the basis of their structural, optical, morphological and photocatalytic properties. Crystallinity of the synthesized materials was confirmed from the X-ray Diffraction (XRD) analysis. Diffuse Reflectance UV–visible (DRUV) and Photoluminescence (PL) spectra of the samples have been recorded to reveal the optical properties of the

synthesized materials. The morphological investigation of the samples was carried out with the help of Field-Emission Scanning Electron Microscopic (FE-SEM) analysis of the samples. The performance of the catalysts was assessed by monitoring the degradation of Methyl Orange (MO) dye under the UV light.

Overall, this paper highlights the advantages of the sonochemical treatment not only for the synthesis but also as a distinct method for novel metal deposition. As compared to other methods, sonochemical method offers more crystallinity, uniformity and thus higher surface area to the nanoparticles at lower temperature.

## 2 Experimental

All the chemicals used were of analytical grade. Titanium isopropoxide was supplied by Avra synthesis Pvt. Ltd. India. Ethanol and Nitric acid used were from Qualigens Pvt. Ltd. India. Glycine and Methyl orange dye were supplied by Loba Chemie Pvt. Ltd. India. Double distilled water was used wherever necessary.

### 2.1 Catalyst Preparation

#### 2.1.1 Sol-Hydrothermal

Stoichiometric amount of Titanium isopropoxide (8 ml) were taken in a beaker and dissolved in appropriate amount of ethanol (33 ml) under vigorous stirring. To this, 2–3 drops of nitric acid were added to obtain a clear solution; the solution was then hydrolyzed with distilled water for 45 min to obtain the sol of TiO<sub>2</sub>. This sol was transferred to a stainless steel autoclave with a Teflon lined container and subjected to hydrothermal treatment under autogeneous pressure for a period of 24 h. The temperature of the autoclave was maintained at 100 °C. The product was washed three times with double-distilled water and dried in an oven at 100 °C for 1 h. The sample synthesized by this method is abbreviated as SH.

#### 2.1.2 Synthesis of TiO<sub>2</sub> by Sol-Hydrothermal Method Using Sonochemically Activated Precursor Solutions

A fixed volume of ethanol (33 ml) was taken in a beaker and kept in a bath type of an ultrasonicator (IMECO, India) at a frequency of  $40 \pm 3$  kHz and 500 W power. The temperature of sonicator was maintained at 30 °C. To this, 8 ml of Titanium isopropoxide was added dropwise with the help of a syringe. Further, 2–3 drops of nitric acid were added to obtain the clear precursor solution followed by dropwise addition of distilled water until a sol of TiO<sub>2</sub> was formed. For synthesis in presence of Glycine, 20 ml of Glycine solution (2 M) was added before the addition

of water. The total time of sonication was around 1 h. The sol thus obtained was then subjected to the hydrothermal treatment described in the previous Sect. (2.1.1). The sample synthesized by this method is abbreviated as SA-SH. Similarly, the sample synthesized in presence of Glycine is abbreviated as SA-SH(GLY).

#### 2.1.3 Synthesis of Ag<sub>2</sub>O Coated TiO<sub>2</sub>

Ag<sub>2</sub>O was deposited on TiO<sub>2</sub> sample [SA-SH(GLY)] by photochemical and sonochemical method. For this, 200 mg of TiO<sub>2</sub> sample was taken in a beaker containing a mixture of distilled water and ethanol (2:1) in a beaker. To this, 5 ml of 0.005 M AgNO<sub>3</sub> was added. This solution was then divided into two parts; one part of this solution was photoirradiated under 80 W high pressure Hg lamp for 2 h in case of photodeposition method [18]. Another part was subjected to sonochemical treatment by keeping it in an ultrasonicator for a period of 2 h. The samples synthesized by photochemical and sonochemical method will be abbreviated as PD-Ag (photochemical method of deposition) and SD-Ag (sonochemical method of deposition) respectively. The coating of Ag<sub>2</sub>O on TiO<sub>2</sub> could be visualized in terms of change in colour of the sample from white to grey black. The reaction mixtures were then filtered, and the products were washed and dried by keeping it in an oven for 3 h at 100 °C.

### 2.2 Characterization

The X-ray diffractograms were recorded on a Bruker AXSD advance X-ray diffractometer with monochromatic Cu K- $\alpha$  radiation ( $\lambda = 1.5406$  Å). Silicon was used as an external standard for correction due to instrumental broadening. FTIR analysis of the samples was carried out in the region 4000–400 cm<sup>-1</sup> on FTIR Shimadzu 8400 instrument. KBr was used as the mulling agent for preparing the samples. The diffuse reflectance UV–visible absorption spectra of the samples were collected on a UV–visible spectrophotometer (Perkin Elmer LAMBDA 950). The photoluminescence (PL) spectra of the solid samples were recorded at room temperature by using PL—Perkin—Elmer LS-55 spectrofluorometer. The spectra were recorded in the range of 375–500 nm with an excitation wavelength of 345 nm. The Field emission micrographs were taken on TESCAN (Model-MIRA 3 LMH) instrument. Energy dispersive X-ray analysis (EDX) samples were performed on an analytical instrument (JEOL-JSM 6360 A). Surface areas of the samples were determined by BET method by using Microtrac specific surface area analyzer.

### 2.3 Photocatalytic Activity

The photocatalytic activities of all the catalysts were tested by studying the degradation reaction of methyl orange (MO). A high pressure mercury lamp (80 W) was used as a light source placed in the photoreactor surrounded with water circulated quartz jacket to avoid thermal heating. Prior to photoreaction, the suspension was magnetically stirred in dark for 30 min to establish adsorption/desorption equilibrium. For a photocatalysis experiment, 0.05 g of the catalyst (powder form) was dispersed in 100 ml of MO (50–100 mg/L) solution. An experimental mixture solution was exposing under the irradiation of visible light source at room temperature before start experimental test run. At optimized interval of reaction time mixture solution were filtered using whatman (0.45 mm) filter paper to separate the various Ag capped TiO<sub>2</sub> (SD-Ag, PD-Ag, and SA-GLY) nanoparticles, afterwards, degraded MO dye solution were examined. The above suspension was kept under constant stirring during visible light irradiation. About 4 ml of aliquots were sampled at regular time intervals, centrifuged to remove particles, and analysed by recording the absorption spectra of methyl orange between 400 and 600 nm using Shimadzu 1800 spectrophotometer [20]. The photo-degradation efficiency of aqueous MO dye during the test run was calculated from Eq. 1 [20].

$$\text{Photo - degradation of MO dye(\%)} = (C_0 - C_e) \times 100 / C_0 \quad (1)$$

where,  $C_0$  and  $C_e$  are the initial and final concentrations (mg/L) of MO dye molecules, respectively.

## 3 Results and Discussion

Synthesis of sonochemically activated TiO<sub>2</sub> was carried out using different mineralizers such as Glycine, Urea, Hexamine and Sodium hydroxide. As only Glycine assisted synthesis leads to the formation of pure anatase phase of TiO<sub>2</sub>, the results for the same are presented in the present paper.

### 3.1 X-ray Diffraction

Figure 1 shows the XRD patterns of TiO<sub>2</sub> samples synthesized by sol-hydrothermal (SH, Fig. 1a) and sonochemically activated sol-hydrothermal method (SA-SH, Fig. 1b). As observed from Fig. 1a, SH sample does not show the formation of TiO<sub>2</sub> phase. On the other hand, SA-SH and SA-SH(GLY), samples show peaks at  $2\theta = 25.3, 38.0, 48.24$  (JCPDS card No. 78–2486) indicating the formation of crystalline anatase phase of TiO<sub>2</sub>. However, SA-SH sample shows an additional small peak at  $2\theta = 30.8$  (marked as # in Fig. 1b, JCPDS card No. 76.1934) corresponding to

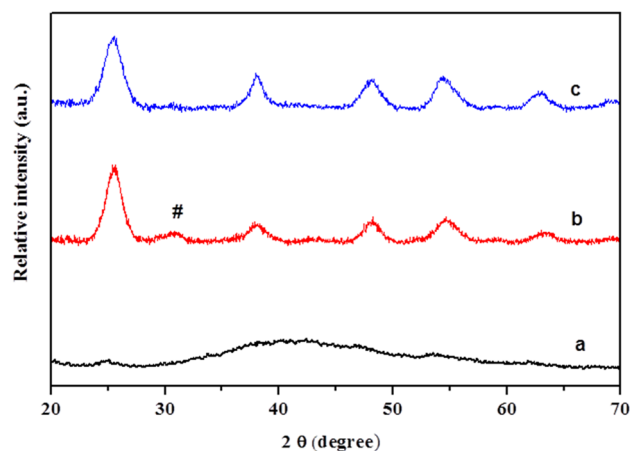
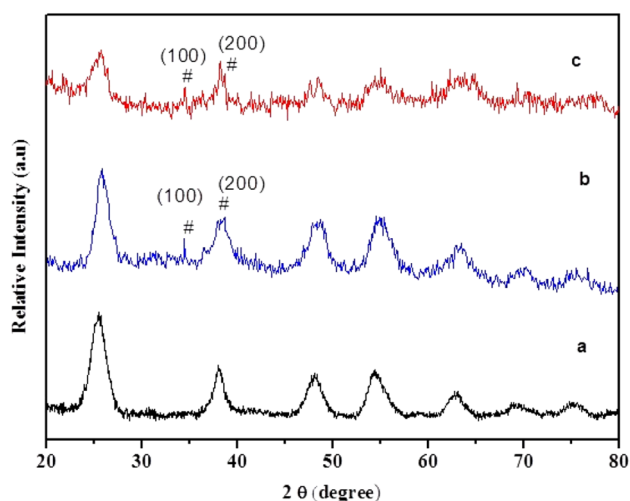


Fig. 1 XRD patterns of (a) SH, (b) SA-SH and (c) SA-SH(GLY)

the brookite phase of TiO<sub>2</sub> which is found to be absent in SA-SH(GLY) sample (Fig. 1c). The formation of crystalline anatase phase at relatively lower temperature (100 °C) after hydrothermal activation for SA-SH and SA-SH(GLY) sample can be attributed to the phenomenon of cavitation accompanied by formation and collapse of millions of vapour bubbles (voids) during sonication. These implosions cause intense local heating (5000 °C) and high pressures (500 atm), within a very short time which facilitate the formation of product (TiO<sub>2</sub>) with a certain crystallinity [19, 20].

However, the high local temperature leads to the formation of small amount of brookite phase of TiO<sub>2</sub> in case of SA-SH sample. This is overcome when the reaction is carried out in presence of glycine. When glycine is used as a mineralizer during the sonochemical activation process, it decomposes into ammonium and hydroxyl ions providing alkaline medium during the synthesis. The basicity suppresses the formation of brookite phase, hence, pure anatase phase can be observed in SA-SH(GLY) sample [21–23]. Further, as SA-SH(GLY) sample shows pure anatase phase, silver coated samples of the same were prepared by using both photochemical (PD-Ag) and sonochemical method (SD-Ag). The XRDs of silver coated samples are shown in Fig. 2 along with that of SA-SH(GLY) sample as a reference. The results suggest that both the deposition processes do not alter the original crystal anatase structure of TiO<sub>2</sub>. However, splitting of TiO<sub>2</sub> peak at  $2\theta = 38.2^\circ$  indicates the presence of silver with the peak at  $\sim 38^\circ$  (JCPDS card No. 04–0783) [24]. The presence of an additional peak appearing at  $2\theta = 34.2^\circ$  reveals that Ag is present as Ag<sub>2</sub>O (JCPDS card No. 41-1104) [25]. The growth of crystal along 100 and 200 planes and the absence of peak corresponding to 111 plane correspond to cubical structure of Ag<sub>2</sub>O nanoparticles [26].

Oxidation of metallic Ag to Ag<sub>2</sub>O is fairly possible as both the deposition processes were carried out under aerobic



**Fig. 2** XRD patterns of (a) SA-SH(GLY), (b) SD-Ag and (c) PD-Ag

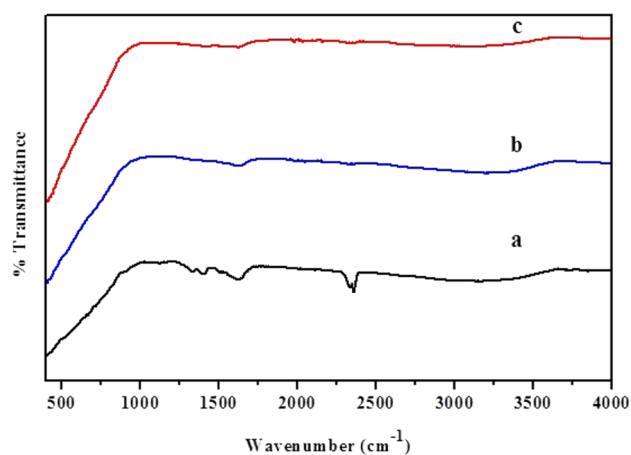


**Fig. 3** FTIR spectra of (a) SA-SH(GLY), (b) PD-Ag and (c) SD-Ag sample

conditions [27, 28]. From Fig. 2, it is to be noted that crystallinity of SD-Ag sample is higher as compared to the PD-Ag sample. It is due to the local agitation profile generated by the sonochemical waves, both on the substrate and in bulk solution [29]. This leads to the formation of smoother layer of crystalline  $\text{Ag}_2\text{O}$  nanoparticles on  $\text{TiO}_2$  surface. Whereas,  $\text{Ag}_2\text{O}$  nanoparticles deposited by photochemical method are found to be amorphous in nature which mask the crystallinity of  $\text{TiO}_2$  nanoparticles.

### 3.2 FTIR

Figure 3 represents the FTIR spectra of bare  $\text{TiO}_2$  [SA-SH(GLY)], SD-Ag, and PD-Ag nanoparticles. The FTIR spectrum of SA-SH(GLY) sample shows prominent bands between 400 and 700  $\text{cm}^{-1}$  corresponding to the

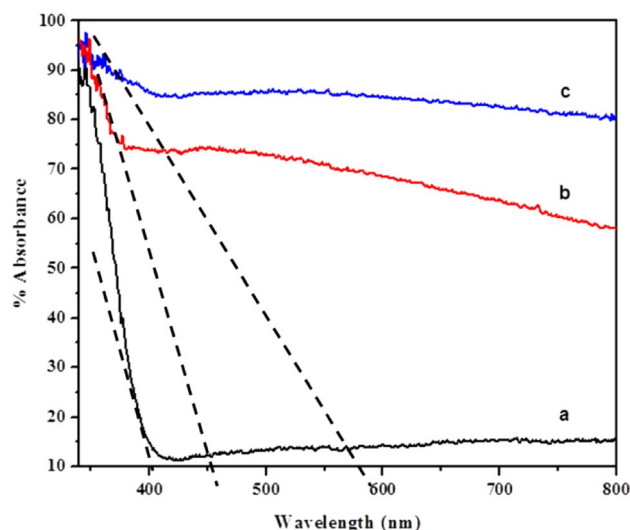


**Fig. 4** Diffuse reflectance UV–visible spectra with band gap calculation of (a) SA-SH(GLY), (b) PD-Ag and (c) SD-Ag

**Table 1** Band gap energies calculated from DRS spectra

Samples	Band gap energies (eV)
$\text{TiO}_2$	3.1
PD-Ag	2.75
SD-Ag	2.1

stretching and bridging vibrations of Ti–O and O–Ti–O bonds respectively [30]. Similarly, a hump at  $\sim 3400 \text{ cm}^{-1}$  and a peak  $\sim 1630 \text{ cm}^{-1}$  represent the stretching vibrations of O–H group and O–H–O groups respectively indicating the presence of physically adsorbed moisture on the surface of the samples. The peaks present at  $\sim 1450 \text{ cm}^{-1}$  correspond to some  $\text{NO}_x$  moieties due to traces of glycine [31]. Figure 3b, c represent the FTIR spectra of PD-Ag and SD-Ag samples which show similar pattern as that of  $\text{TiO}_2$  with peaks corresponding to  $\text{NO}_x$  moieties being absent in both the samples which could be due to the degradation of these moieties during the photochemical and sonochemical deposition processes.

### 3.3 DRUV

DRUV spectra of bare  $\text{TiO}_2$  (SA-SH(GLY)) and silver coated samples are given in Fig. 4. The approximate band gap values of these samples (calculated from these spectra) are found (Table 1) to be 3.1, 2.75 and 2.1 eV for (SA-SH(GLY), PD-Ag and SD-Ag samples respectively). These values indicate that the band gap values of  $\text{TiO}_2$  decreased significantly after coating with the  $\text{Ag}_2\text{O}$  nanoparticles. Thus, silver coated samples (Fig. 4b, c) show enhancement in the visible



light absorption as compared to bare  $\text{TiO}_2$  sample (Fig. 4a). Moreover, the intensity of SD-Ag (Fig. 4c) sample is found to be higher than PD-Ag sample (Fig. 4b). The higher intensity of the SD-Ag sample can be attributed to the microjets and shockwaves created after the collapse of the bubbles or cavities resulting in highly energetic impingement of the nanoparticles towards the  $\text{TiO}_2$  particles, during sonication [32]. This increases the nucleation density of  $\text{Ag}_2\text{O}$  on  $\text{TiO}_2$  surface thereby yielding homogeneous coating compared to that of photochemical method.

### 3.4 Photoluminescence Spectra

The typical photoluminescence (PL) spectra of the  $\text{TiO}_2$  samples [SA-SH(GLY)] as a representative, along with the silver deposited samples are shown in Fig. 5. The spectra were recorded by using an excitation wavelength of 345 nm. As observed from the Fig. 5, SA-SH(GLY) sample exhibits intense emission spectrum with peaks at ~395, 415, 448, 472, 480 and 522 nm wavelengths compared to  $\text{Ag}_2\text{O}$  coated samples. The strong peak at about 395 nm can be correlated to the emission of band gap transition of anatase phase of  $\text{TiO}_2$ . The oxygen vacancies and surface hydroxyl groups of  $\text{TiO}_2$  serve as sites of recombination as trapped electrons and holes can be easily captured by these sites.

The emissions that occur from these recombinations contribute to the visible light emissions. In contrast to this, the silver deposited samples exhibit PL spectra with poor intensities. When  $\text{Ag}_2\text{O}$  nanoparticles are deposited on the surface of the catalyst, electronic interaction occurs between  $\text{Ag}_2\text{O}$  and  $\text{TiO}_2$ . Photoexcited electrons in the conduction band of  $\text{TiO}_2$  can be effectively trapped by the  $\text{Ag}_2\text{O}$  nanoparticles. This electron transfer would inhibit the recombination of electron–hole pairs leaving holes in

the valence band of  $\text{TiO}_2$  resulting in lower rate of recombinations of charge carriers [33, 34]. In case of coated samples, SD-Ag sample appears to be better in comparison to PD-Ag sample due to higher degree of crystallinity and hence lower defect concentration [35, 36].

### 3.5 FE-SEM and EDX

Figure 6 depicts the surface morphology of bare  $\text{TiO}_2$  [SA-SH(GLY)] and Ag coated samples (SD-Ag and PD-Ag). Figure 6a–c are taken at 100 k $\times$  magnification whereas d, e and f are taken at 300 k $\times$  magnification. As observed from the micrographs, SA-SH(GLY) sample (Fig. 6 a, d) exhibits fine particles of 2–3 nm size bearing spherical morphology. On the contrary, silver coated samples (Fig. 6b, c) show particles with a relatively larger size distribution (30–50 nm) with different morphologies. The photo-deposited  $\text{Ag}_2\text{O}$  nanoparticles (PD-Ag) show cubical particles while the  $\text{Ag}_2\text{O}$  particles in sonochemically deposited (SD-Ag) sample appear to be spherical in shape. However, when observed under higher magnification both the samples (Fig. 6e, f) appear to be cubical in shape except that the particles in PD-Ag sample bear sharp edges while in the SD-Ag sample the particles are seen to have etched corners. This transformation can be justified as follows: during the sonochemical deposition process, as highly energetic ultrasound waves are continuously bombarded, the water molecules surrounding the  $\text{Ag}_2\text{O}$  crystals undergo decomposition forming hydrogen and hydroxyl radicals. These ultrasonic waves together with oxidative radicals bring about the oxidative etching (in which oxygen radicals in bulk solution dissolve the surface atoms especially at edges and corners) of the corners of the  $\text{Ag}_2\text{O}$  cubes [37–39].

The elemental analysis (Table 2) by EDX confirmed the presence of  $\text{Ag}_2\text{O}$  on both the SD-Ag and PD-Ag samples. The concentration of  $\text{Ag}_2\text{O}$  is found to be 0.71% and 0.65% for SD-Ag and PD-Ag samples respectively.

### 3.6 $\text{N}_2$ -BET Surface Area

The surface area of pure  $\text{TiO}_2$  [SA-SH(GLY)], PD-Ag and SD-Ag samples are calculated by the Brunauer–Emmett–Teller (BET) method were 105.34, 100 and 79  $\text{m}^2\text{g}^{-1}$ , respectively. The lower surface area of SD-Ag and PD-Ag samples is due to the deposition of Ag nanoparticles which covered some mesoporous and interstitial space of the  $\text{TiO}_2$  network [40].

The higher surface area value of SD-Ag sample than the PD-Ag sample can be attributed to uniform distribution of  $\text{Ag}_2\text{O}$  nanoparticles and their rounded cube like morphology.

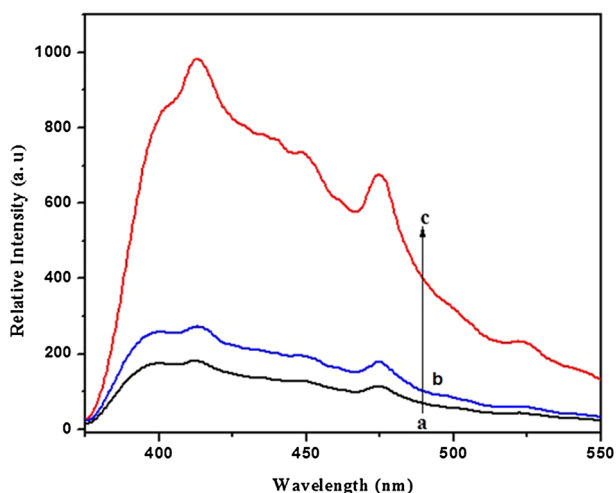


**Fig. 5** Photoluminescence spectra of (a) SD-Ag, (b) PD-Ag and (c) SA-SH(GLY)

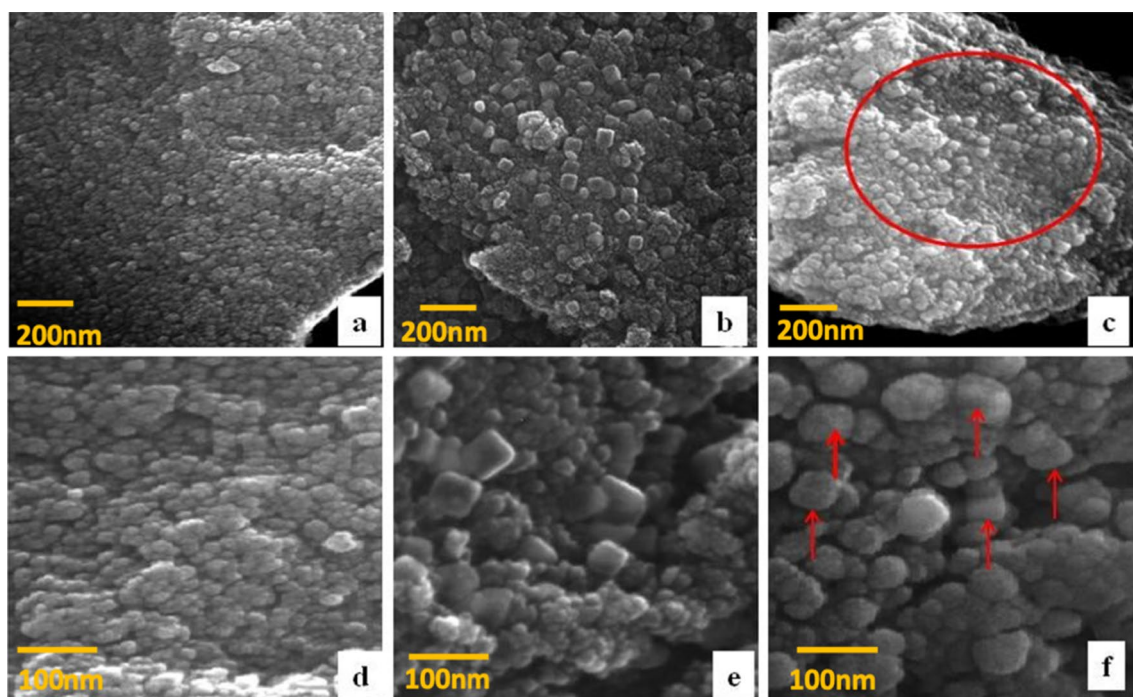


**Fig. 6** FE-SEM of **a, d** SA-SH(GLY), **b, e** PD-Ag and **c, f** SD-Ag samples

**Table 2** EDX elemental analysis

Sample	Elemental %		
	Ti	O	Ag
SA-SH(GLY)	43.26	56.45	–
PD-Ag	24.82	74.14	0.65
SD-Ag	21.12	78.20	0.71

### 3.7 Photocatalytic Activity

The photocatalytic activities of the synthesized catalysts were evaluated by studying the photodegradation of methyl orange (MO). Figure 7 shows the equilibration time for MO dye removal from MO contaminated aqueous waste under UV light irradiation onto the various  $\text{Ag}_2\text{O}$  co-capped  $\text{TiO}_2$  (SD-Ag, PD-Ag, and SA-GLY) nanoparticles. The initial concentration of MO dye was varied from 50 to 100 mg/L, the reaction solution was 100 mL and the amount of photocatalysts 0.05 g. The photo-degradation efficiency significantly improved for the initial 30 min and then gradually increased. Equilibrium of MO dye removal was achieved within about 90 min with removal efficiencies of 99.9, 67.1, and 44.4% for SD-Ag, PD-Ag, and SA-GLY nanoparticles, respectively at 50 mg/L of MO dye concentration (Fig. 7a). As observed from Fig. 7a, the sequence of activities is observed as SD-Ag > PD-Ag > SA-SH(GLY). The efficiency of photocatalysts is governed by several factors

like crystallinity, rate of recombinations, surface area and electronic structure of surface states. Higher photoactivities of coated samples than the bare  $\text{TiO}_2$  i.e. SA-SH(GLY) can be ascribed to the enhanced charge separation. In case of  $\text{Ag}_2\text{O}$  coated samples, SD-Ag sample seems to be more photoactive. The higher activity of SD-Ag sample can be attributed to the improved properties like crystallinity, visible light absorption capacity and higher surface area [41, 42]. The effect of time interval for kinetics study of MO dye photo-degradation is demonstrated in Fig. 7b with the pseudo-first order reaction shown in Eq. 2 [42].

$$\ln(C_0/C_t) = Kt \quad (2)$$

where, at a time “t”,  $C_0$  and  $C_t$  are the initial and final concentrations of MO polluted aquatic waste, respectively (mg/L). The reaction rate constant  $K$  ( $\text{min}^{-1}$ ) was calculated by the linear graph of  $\ln(C_0/C_t)$  vs. “t” (Fig. 7b). The reaction rate constant increased from 0.5761 to 0.7649 up to 100 mg/L with increasing MO dye pollution concentration (Table 3).

Figure 7c depicts two peaks at ( $t_R = 14.2$  and  $12.3$  min) corresponding to methyl orange for an irradiated solution (Curve a). After the time interval of 60 min, there is a significant shift ( $t_R = 13.7$  and  $11.7$  min) in the retention time of MO. As the reaction progresses, one can observe a substantial decrease in the intensity of the peaks corresponding to MO with slight shift in the retention time. The shift in

**Fig. 7** **a** Reaction time effect and, **b** first order reaction rate of the MO dye photodegradation by SD-Ag sample (MO dye concentration of 50–100 mg/L, Photocatalyst dose of 0.05 g, reaction volume of 100 mL, reaction temperature of 35 °C), **c** HPLC profiles of the MO dye in presence of SD-Ag sample at (a) 0 min (b) 60 min (c) 90 min (d) 120 min

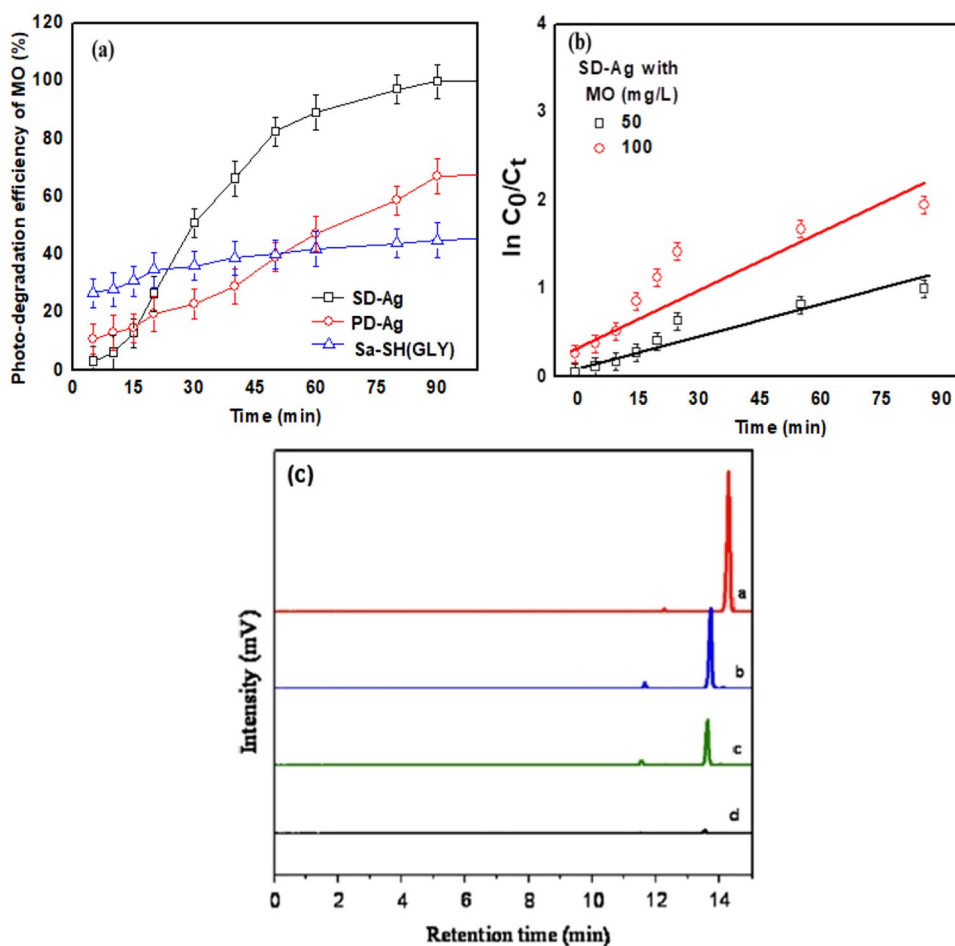


**Table 3** Pseudo-first order rate constants for MO dye photo-degradation by SD-Ag sample different initial concentrations

MO dye (mg/L)	K (min <sup>-1</sup> )	R <sup>2</sup>
50	0.5761	0.984
100	0.7649	0.946

retention time can be attributed to the hydroxylated species of MO formed during the degradation reaction which show lower retention time [42–44]. The decrease in the intensity values of the peak implies almost 100% degradation of the MO together with the decoloration. Similar curves have been obtained for the MO dye irradiated in the presence of other photocatalyst. These curves indicate the complete mineralization of MO dye.

The high photo-degradation activity of the samples containing Ag was explained by hypothesizing the mechanism reported in Fig. 8. The MO dye contains two azo bonds and its degradation depends on produced hydroxyl radicals and super oxide anion radical under illumination. Under visible light illumination electron–hole pairs are generated and must be separated for degradation reactions. Holes react

with surface adsorbed hydroxyl ions and form hydroxyl free radical oxidizing dye molecule. However, chances of electron–hole recombination are very high. High catalytic activity of Ag<sub>2</sub>O co-capped TiO<sub>2</sub> (SD-Ag) sample indicates better charge separation. Silver may trap photoexcited electron and reduce the chances of recombination with holes. It is also reported potential difference at junction promotes the charge separation and thus, may increase the photo-catalytic activity [43–47].

### 4 Conclusions

Nanocrystalline TiO<sub>2</sub> samples were successfully synthesized by SH method using sonochemically activated precursor solutions. Prior sonochemical activation of precursors yielded anatase phase of TiO<sub>2</sub> as a final product with small amount of brookite phase at relatively lower temperature (100 °C) with desirable crystallinity. Addition of glycine during sonochemical activation resulted in the formation of pure anatase phase of TiO<sub>2</sub>. The pure anatase phase TiO<sub>2</sub> sample was further coated with Ag<sub>2</sub>O nanoparticles



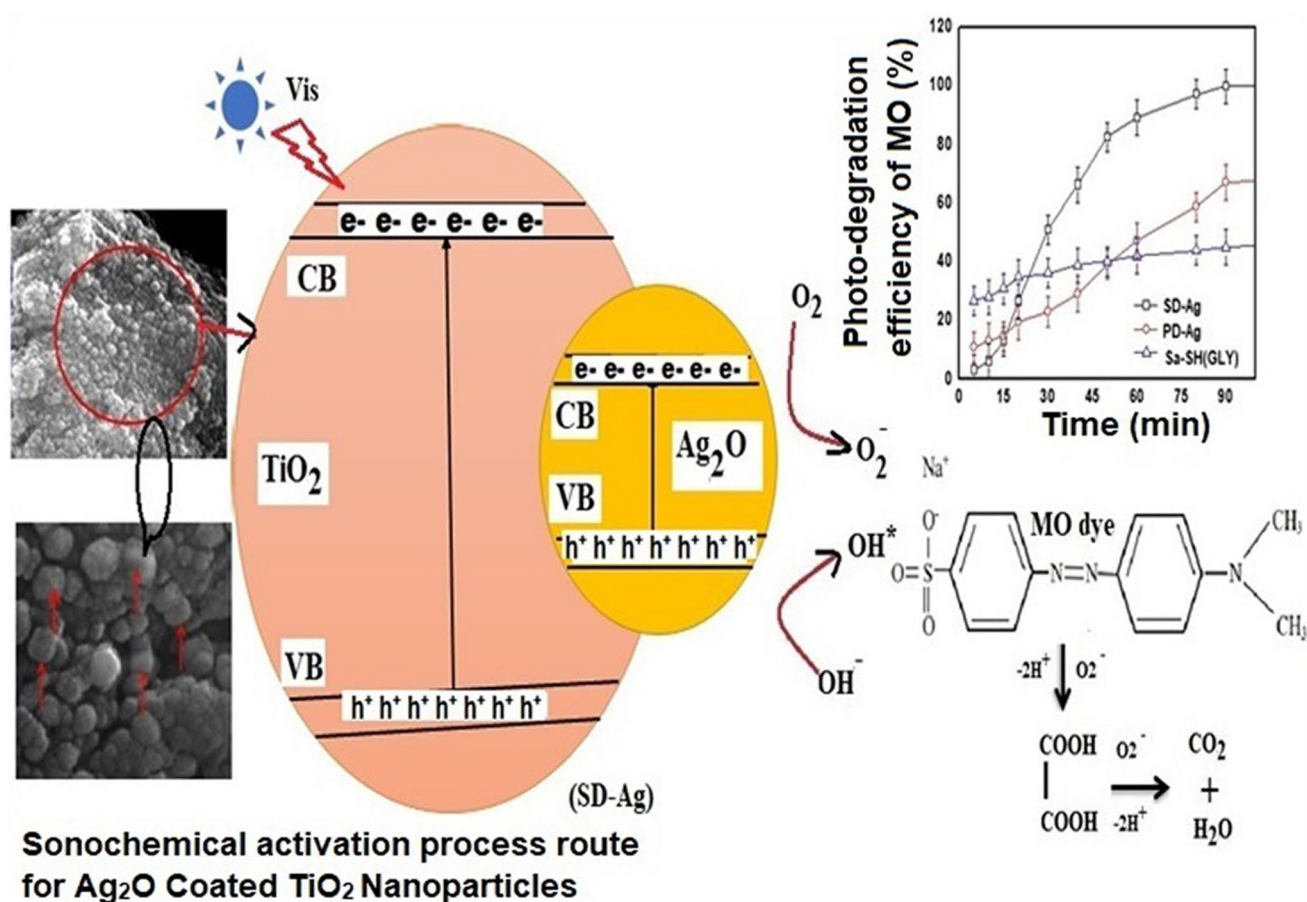


**Fig. 8** Proposed mechanism for photo-catalytic of SD-Ag sample for photo-degradation of MO under UV irradiation

employing sonochemical and photochemical methods of deposition. Sonochemically deposited product is found to exhibit higher crystallinity, surface area and improved optical and morphological properties which contributes in the higher photoactivity of the sample than the photochemically deposited sample. Equilibrium of MO dye removal was achieved within about 90 min with removal efficiencies of 99.9, 67.1, and 44.4% for SD-Ag, PD-Ag, and SA-GLY nanoparticles, respectively at 50 mg/L of MO dye concentration. The efficient photo-catalytic activity of SD-Ag sample was observed for MO photo-degradation, which is attributed to the improved properties like crystallinity, visible light absorption capacity and higher surface area. High catalytic activity of Ag<sub>2</sub>O co-capped TiO<sub>2</sub> (SD-Ag) sample indicates better charge separation.

**Acknowledgements** The funding for this work has been provided by Bhabha Atomic Research Center (BARC), Mumbai. AAB acknowledges BARC for SRF. The authors gratefully acknowledge CNQS, Department of Physics, University of Pune for XRD analysis, SAIF, ICT Mumbai for FESEM analysis.

## References

- Schneider J, Matsuoka M, Takeuchi M, Zhang J, Horiuchi Y, Anpo M, Bahnemann DW (2014) *Chem Rev* 114:9919–9986
- Wu B, Liu D, Mubeen S, Chuong T, Moskovits M, Stucky GD (2016) *J Am Chem Soc* 138:1114–1117
- Dong R, Zhang Q, Gao W, Pei A, Re B (2016) *ACS Nano* 10:839–844
- Xu Y, Lotfabad EM, Wang H, Farbod B, Xu Z, Kohandehghan A, Mitlin D (2013) *Chem Commun* 49:8973–8975
- Lu Q, Lu Z, Lu Y, Lv L, Ning Y, Yu H, Hou Y, Yin Y (2013) *Nano Lett* 13:5698–5702
- Velasco LF, Haro M, Parmentier J, Gadiou R, Guterl CV, Ania CO (2013) *J Catal*. <https://doi.org/10.1155/2013/178512>
- Zhang Y, Zhang S, Wang K, Ding F, Wu J (2013) *J Nanomater*. <https://doi.org/10.1155/2013/294020>
- Wang B, Guo L, Hea M, He T (2013) *Phys Chem Chem Phys* 15:9891–9898
- Bacsa R, Kiwi J, Ohno T, Albers P, Nadochenko V (2005) *J Phys Chem B* 109:5994–6003
- Parida KM, Sahu N, Tripathi AK, Kambale VS (2010) *Environ Sci Technol* 44:4155–4160
- Yang XH, Li Z, Sun C, Yang HG, Li C (2011) *Chem Mater* 23:3486–3494

12. Wang Y, Zhang L, Li S, Jena P (2009) *J Phys Chem C* 113:9210–9217
13. Nedelcheva AD, Iordanova RS, Stoyanova AM, Gegova RG, Dimitriev YB, Loukanov AR (2013) *Cent Eur J Chem* 11:364–370
14. Periyat P, Leyland N, McCormack D, Colreavy J, Corr D, Pillai S (2010) *J Mater Chem* 20:3650–3655
15. Neppolian B, Bruno A, Bianchi CL, Ashokkumar M (2012) *Ultrason Sonochem* 19:9–15
16. Wang CC, Ying JY (1999) *Chem Mater* 11:3113–3120
17. Huang W, Tang X, Wang Y, Koltypin Y, Gedanken A (2000) *Chem Commun*. <https://doi.org/10.1039/B003349I>
18. Yang YF, Sangeetha P, Chen YW (2009) *Int J Hydrogen Energy* 34:8912–8920
19. Meskin PE, Ivanov VK, Barantchikov AE, Churagulov BR, Tretyakov YD (2006) *Ultrason Sonochem* 13:47–53
20. Abbasi AR, Morsali A (2010) *Ultrason Sonochem* 17:704–710
21. Tao YG, Xu YQ, Pan J, Gu H, Qin CY, Zhou P (2012) *Mat Sci Eng B* 177(1664):1671
22. Nagaveni K, Hegde MS, Ravishankar N, Subbanna GN, Madras G (2004) *Langmuir* 20:2900–2907
23. Cheng H, Ma J, Zhao Z, Qi L (1995) *Chem Mater* 7:663–671
24. Wang X, Huang P, Feng L, He M, Guo S, Shen G, Cui D (2012) *RSC Adv* 2:3816–3822
25. Raju NRC, Kumar KJ, Subrahmanyam A (2009) *J. Phys. D Appl. Phys.* 42:135411
26. Lyu LM, Wang WC, Huang MH (2010) *Chem Eur J* 16:14167–14174
27. Zhang H, Wang G, Chen D, Lv X, Li J (2008) *Chem Mater* 20:6543–6549
28. Zhou W, Liu H, Wang J, Liu D, Du G, Cui J (2010) *ACS Appl Mater Interfaces* 2:2385–2392
29. Gedanken A (2004) *Ultrason Sonochem* 11:47–55
30. Parida KM, Sahu N (2008) *J Mol Catal A Chem* 287:151–158
31. Huang DG, Lia SJ, Zhou WB, Quan SQ, Liu L, He ZJ, Wan JB (2009) *J Phys Chem Solids* 70:853–859
32. Kim SD, Choe WG, Jeong JR (2013) *Ultrason Sonochem* 20:1456–1462
33. Li C, Hsieh JH, Cheng JC, Huang CC (2014) *Thin Solid Films* 570:436–444
34. Wu M, Yan JM, Zhao M, Jiang Q (2012) *Chem Plus Chem* 00:1–6
35. Tian G, Fu H, Jing L, Tian C (2009) *J Haz Mat* 161:1122–1130
36. Wu J, Lü X, Zhang L, Xia Y, Huang F, Xu F (2010) *J Alloys Compd* 496:234–240
37. Kim MJ, Cho YS, Park SH, Huh YD (2012) *Cryst Growth Des* 12:4180–4185
38. Xiong Y (2011) *Chem Commun* 47:1580–1582
39. Ma Y, Li W, Zeng J, McKiernan M, Xie Z, Xia Y (2010) *J Mater Chem* 20:3586–3589
40. Zada I, Zhang W, Zheng W, Zhu Y, Zhang Z, Zhang J, Imtiaz M, Abbas W, Zhang D (2017) *Sci Rep* 7:17277
41. Sharma A, Thuan DV, Pham TD, Tung MHT, Truc NTTTT, Vo D-VN (2020) *Chem Eng Technol* 43(4):1–11
42. Sharma A, Lee BK (2014) *Appl Surf Sci* 313:624–632
43. Sharma A, Lee BK (2017) *Catal Today* 298:158–167
44. Sharma A, Lee BK (2017) *Catal Today* 287:113–121
45. Sharma A, Lee BK (2020) *J. Compos. Mater.* 10:113–121
46. Mohapatra S, Singha J, Satpati B (2020) *J Phys Chem Solids* 138:109305
47. Ren HT, Han J, Li TT, Jia FS, Lin H, Lou CW (2019) *J Photochem Photobiol A* 377:260–267

**Publisher's Note** Springer Nature remains neutral with regard to jurisdictional claims in published maps and institutional affiliations.